

1 Search for Anomalous Production of Photon + Jets
2 + Missing Transverse Energy in $p\bar{p}$ Collisions at
3 $\sqrt{s} = 1.96$ TeV Using the CDF II Detector

4
5 April 21, 2011

6 **Abstract**

7 A model-independent signature-based search for physics beyond the Standard
8 Model is performed in the photon + jets + missing transverse energy channel in
9 $p\bar{p}$ collisions at a center of mass energy of 1.96 TeV using the CDF II detector.
10 Events with a photon + jets are predicted by the Standard Model and also by
11 many theoretical models beyond the Standard Model. In the Standard Model,
12 the main mechanisms for photon + jets production include quark-antiquark an-
13 nihilation and quark-gluon scattering. No intrinsic missing transverse energy is
14 present in any of these Standard Model processes. In this search, photon + ≥ 1
15 jet and photon + ≥ 2 jet events are analyzed with and without a minimum re-
16 quirement on the missing transverse energy. Numerous mass distributions and
17 kinematic distributions are studied and no significant excess over the background
18 prediction is found. All results indicate good agreement with expectations of the
19 Standard Model.

1 Introduction

We present the findings of a model-independent, signature-based search for anomalous photon (γ) + jets events from $p\bar{p}$ collisions at $\sqrt{s} = 1.96$ TeV using 4.8 fb^{-1} of data recorded by the upgraded Collider Detector at Fermilab (CDF II) [1]. In $\gamma + \geq 1$ jet events and $\gamma + \geq 2$ jet events, we measure a variety of kinematic distributions including the transverse energy (E_T) of the photon, the transverse energy of the leading jet(s), the invariant mass of the photon + leading jet(s), the invariant mass of the two leading jets, and the total transverse energy in the event (H_T). The shapes of these distributions are examined for deviations from expectations based on Standard Model (SM) processes and other backgrounds.

The Feynman diagrams in Fig. 1(a) and 1(b) illustrate examples of processes that yield the $\gamma + 2$ jets signature. It is interesting to search for a discrepancy in a variety of kinematic distributions because a resonance or excess could hint at the existence of a new heavy particle decaying into $\gamma + \text{jets}$, or a new physics mechanism such as gauge-mediated SUSY breaking (GMSB) [2] or Technicolor [3]. Of particular interest are events with large missing E_T (\cancel{E}_T), since many new physics models predict the existence of particles that would evade detection and produce an imbalance of transverse energy; for example, a Gravitino (\tilde{G}) produced in a Neutralino decaying to $\tilde{\chi}_1^0 \rightarrow \gamma \tilde{G}$. Standard Model $\gamma + \text{jets}$ processes have no intrinsic \cancel{E}_T .

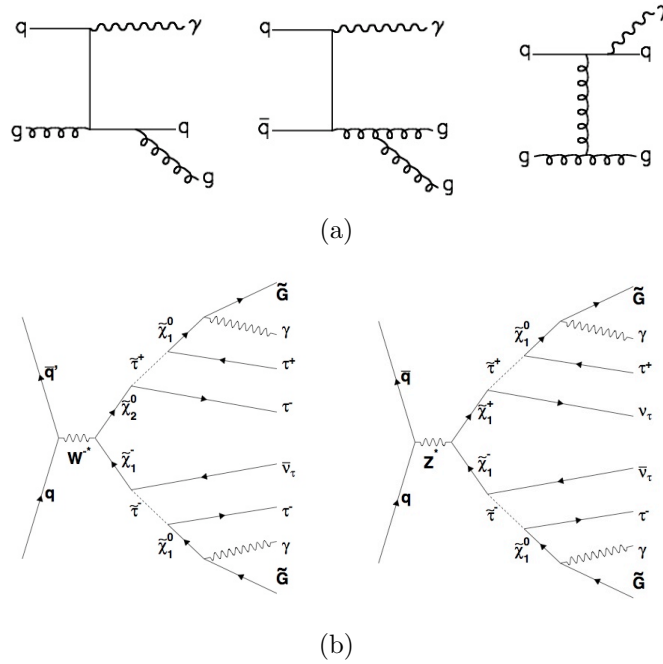


Figure 1: Feynman diagrams for tree-level (a) Standard Model and (b) GMSB processes that yield the $\gamma + 2$ jets signature. The Standard Model processes have no intrinsic \cancel{E}_T . A SUSY-like signal may be observed in $\gamma + \text{jets}$ events with large \cancel{E}_T .

1 We present two different methods of determining the backgrounds. In the first
2 method (Method A), we rely on a leading-order Monte Carlo generator (PYTHIA) to
3 predict the kinematic properties of jets in SM $\gamma + \text{jets}$ events. In the second method
4 (Method B), we employ a novel weighting technique that uses a combination of data and
5 Monte Carlo to model higher-order QCD effects in kinematic distributions involving
6 jets.

7 **2 CDF II Detector**

8 The Collider Detector at Fermilab (CDF) is general purpose detector [1]. It has a
9 tracking system lying next to the beam pipe which is immersed in a superconducting
10 solenoidal magnet providing a uniform 1.4 T magnetic field. The amount and the
11 direction of a deflected charged particle is used to infer its momentum and charge.
12 Outside of the solenoid are the calorimeters, which measure the energy of particles
13 produced in the collision.

14 The tracking system comprised of a silicon pixel detector and open-cell drift cham-
15 ber, central outer tracker (COT). The silicon detector and COT provides particle track
16 information and the location of primary and secondary interaction points. The sili-
17 con system provides up to 8 measurements in the $r - \phi$ and $r - z$ views and covers
18 the track reconstruction in the region $|\eta| < 2$. The COT makes up to 96 measure-
19 ments along the track of of each charge article in the region $|\eta| < 1$. Sense wires
20 are arranged in 8 alternating axial and $\pm 3^\circ$ stereo super-layers. The resolution in
21 p_T , σ/p_T , is $\approx 0.0015 p_T \cdot \text{GeV}^{-1} \cdot c$ for track with only COT measurements, and
22 $\approx 0.0007 p_T \cdot \text{GeV}^{-1} \cdot c$ for tracks with both the silicon and the COT measurements.
23 The calorimeter has two electromagnetic (EM) section and a hadronic section to stop
24 and measure both EM and hadronic particles. It has a projective tower geometry and
25 is tower-segmented. The Central Preshower detector (CPR) lies after the drift cham-
26 ber on the surface of the central calorimeter. CPR detector samples the early particle
27 shower and improves photon identification and energy resolution. The Central Electro-
28 magnetic Shower Maximum detector (CES) is embedded in the central electromagnetic
29 calorimeter and sample the lateral shower of the particle. It aids in separating neutral
30 meson (π^0 , η) decays from prompt photons.

31 CDF detector has a tower segmented calorimeter arranged in a projective geometry.
32 Each calorimeter tower consists of an electromagnetic and a hadronic compartments
33 [10]. The central calorimeter covers the region $|\eta| < 1.1$ and the ‘end plug’ region
34 extends from $1.1 < |\eta| < 3.6$. The central calorimeter is segmented in to 15° in
35 ϕ and ≈ 0.1 in η and has an E_T resolution of $\sigma(E_T)/E \approx 13.5\% \sqrt{E_T/\text{GeV}} \oplus 2\%$
36 and the plug electromagnetic calorimeter has an energy resolution of $\sigma(E_T)/E_T =$
37 $16.0\%/\sqrt{E_T} \oplus 2\%$. The central hadron calorimeter and plug hadron calorimeter energy
38 resolution is $50\% \sqrt{E} \oplus 3\%$ and $80\% \sqrt{E} \oplus 5\%$ respectively.

39 CDF uses a cylindrical coordinate system with the z -axis along the axis of the
40 colling beams. The variable θ is the polar angle relative to the incoming proton beam,

1 and the variable ϕ is the azimuthal angle about the beam axis. The pseudorapidity of
2 a particle trajectory is defined as $\eta = -\ln(\tan(\theta/2))$. It is also useful to define detector
3 pseudorapidity η_{det} , denoting a particle's pseudorapidity in a coordinate system in
4 which the origin lies at the center of the CDF detector rather than the at the event
5 vertex. The transverse momentum p_T is the component of the momentum projected
6 on a plane perpendicular to the beam axis.

7 3 Data Sample and Event Selection

8 We select a sample of γ candidates by identifying isolated electromagnetic clusters with
9 $E_T > 30$ GeV in the central region of the central calorimeter ($|\eta^{\text{detector}}| < 1.1$). In ad-
10 dition, we require the EM cluster to pass standard photon selection requirements [4].
11 To reduce the background from charged leptons, we require an absence of tracks point-
12 ing in the direction of the EM cluster. The background from cosmic rays is reduced
13 with a requirement on calorimeter EM timing [5], and we remove events that origi-
14 nate from the beam halo using a set of topological selection requirements [6]. Events
15 with photomultiplier tube spikes — an instrumentation effect that can resemble a γ
16 — are also removed. In the remaining event sample, we identify one or more jets with
17 $E_T > 15$ GeV and $|\eta^{\text{detector}}| < 3.0$. Jet energies are corrected for detector response,
18 energy loss, multiple $p\bar{p}$ interactions and the underlying event [7]. Furthermore, an
19 azimuthal separation of $\Delta\phi > 0.4$ radians between the direction of \cancel{E}_T and any jet
20 above $E_T > 15$ GeV is used to improve the energy measurement of jets.

21 After applying the event selection requirements described above, we select two
22 data samples based on the number of jets with $E_T > 15$ GeV: $\gamma + \geq 1$ jet events and
23 $\gamma + \geq 2$ jet events. Within these two samples, subsamples with $\cancel{E}_T > 20$ GeV are iden-
24 tified. By selecting events with large \cancel{E}_T , the dominant SM γ and jet backgrounds are
25 reduced, hence increasing our sensitivity to new physics. Various kinematic distribu-
26 tions in each of the four data samples are compared to the background expectation.

27 4 Modeling Backgrounds

28 In this analysis we model backgrounds from two main sources: SM processes and non-
29 collision processes. The SM processes include (1) prompt γ production, (2) prompt
30 diphoton production, (3) electroweak production of charged leptons that fake a prompt
31 photon, and (4) QCD production of hadronic jets that fake a prompt photon. The non-
32 collision processes include energetic particles from cosmic rays and the beam halo that
33 mimic the signal of a prompt photon from a $p\bar{p}$ collision. The PYTHIA Monte Carlo
34 generator (Tune A) [8] is used to model SM prompt γ production, prompt diphoton
35 production, and the electroweak charged lepton backgrounds. All other backgrounds
36 are modeled using data. For each of these SM backgrounds and the non-collision
37 background, we construct a background template for each of the kinematic distributions
38 under investigation. The sum of these background templates is then compared to data.

SM diphotons are a significant source of fake \cancel{E}_T background, as the probability to lose one of the photons in an uninstrumented region of the detector is twice as large as in a photon + jet event. The electroweak background is mainly from W , Z , WW , WZ , and ZZ production, in which a final state lepton radiates a photon and we identify it as the prompt photon.

The background from QCD multijet production, in which a jet fakes a photon, is modeled using a sample that consists of jets that pass looser photon selection requirements (“sideband” events). These jets are from neutral mesons like π^0 and η which decay almost exclusively to several photons. These energetic photons cannot be resolved well and are reconstructed as a single isolated photon.

Although a large portion of non-collision backgrounds from cosmic rays and the beam halo is removed by the γ + jets selection requirements, some events remain, and these backgrounds are significant in the large \cancel{E}_T subsamples. A pure cosmic ray event sample is attained using calorimeter EM timing information and is used to construct the background template. A set of topological cuts is used to select beam halo events.

We employ two different methods to construct templates from these background sources. In both methods, the SM diphoton and SM charged lepton background templates are normalized to the expected number of events in the γ + jets data using their respective Monte Carlo production cross sections and the integrated luminosity of the data. The cosmic ray and beam halo templates are normalized to the expected number of background events in the γ + jets data. The two methods differ in their treatment of the SM γ background and the QCD multijet background, as described below.

Method A: We model the SM prompt γ production using the PYTHIA Monte Carlo generator and the QCD multijet background from sideband events. In Method A, these two background templates are scaled so that the total number of SM γ events ($N^{\text{SM}\gamma}$) and the total number of QCD multijet events (N^{QCD}) satisfy

$$N^{\text{QCD}} = f \cdot (N^{\text{SM}\gamma} + N^{\text{QCD}}), \quad (1)$$

where f is the fake photon fraction, which is determined to be

$$f = 0.319 \pm 0.001(\text{stat}) \pm 0.0068(\text{syst}) \quad (2)$$

from a study of inclusive photon data with photon $E_T > 30$ GeV [4]. In addition, the overall normalization of the SM γ and QCD templates is adjusted so that the total number of background events from all sources equals the number of observed events in the data:

$$N^{\text{Data}} = N^{\text{SM}\gamma} + N^{\text{QCD}} + \underbrace{N^{\text{Di-}\gamma}}_{\text{fixed}} + \underbrace{N^{\text{EWK}}}_{\text{fixed}} + \underbrace{N^{\text{Non-collision}}}_{\text{fixed}}. \quad (3)$$

When used together, Eqs. 1 and 3 uniquely determine $N^{\text{SM}\gamma}$ and N^{QCD} . We note that since the total number of events in the templates is constrained to match the total number of events in the data, our kinematic distributions are not sensitive to anomalies in the overall number of γ + jets events, but they are sensitive to anomalies in the shapes of the distributions and excesses in the tails.

1 Table 1 summarizes the Method A background estimates for the $\gamma + \geq 1$ jet and
2 $\gamma + \geq 2$ jet samples. Table 2 summarizes the Method A background estimates for the
3 $\gamma + \geq 1$ jet + $\cancel{E}_T > 20$ GeV and $\gamma + \geq 2$ jet + $\cancel{E}_T > 20$ GeV samples.

Background	$\gamma + \geq 1$ Jet Sample	$\gamma + \geq 2$ Jet Sample
Prompt γ	$3387044 \pm 1840 \pm 108938$	$629569 \pm 793 \pm 39721$
QCD	$1472467 \pm 1213 \pm 27108$	$273681 \pm 523 \pm 6095$
Electroweak	$11765 \pm 108 \pm 952$	$1833 \pm 42 \pm 271$
Diphoton	$12136 \pm 110 \pm 641$	$1775 \pm 42 \pm 196$
Non-Collision	$132 \pm 11 \pm 4$	$8 \pm 2 \pm 1$
$\gamma + \text{jets Data}$	4883544 ± 2209	906866 ± 952

Table 1: Summary of background estimates for the $\gamma + \geq 1$ jet and $\gamma + \geq 2$ jet data samples evaluated by Method A. Where two uncertainties are quoted, the first is statistical and the second is systematic.

Background	$\gamma + \geq 1$ Jet + $\cancel{E}_T > 20$ GeV Sample	$\gamma + \geq 2$ Jet + $\cancel{E}_T > 20$ GeV Sample
Prompt γ	$88878 \pm 366 \pm 3178$	$28502 \pm 168 \pm 1429$
QCD	$38527 \pm 196 \pm 1664$	$12385 \pm 111 \pm 524$
Electroweak	$6271 \pm 79 \pm 613$	$843 \pm 29 \pm 122$
Diphoton	$355 \pm 19 \pm 13$	$86 \pm 9 \pm 8$
Non-Collision	$124 \pm 12 \pm 4$	$8 \pm 3 \pm 1$
$\gamma + \text{jets Data}$	134155 ± 366	41824 ± 204

Table 2: Summary of background estimates for the $\gamma + \geq 1$ jet + $\cancel{E}_T > 20$ GeV and $\gamma + \geq 2$ jet + $\cancel{E}_T > 20$ GeV data samples evaluated by Method A. Where two uncertainties are quoted, the first is statistical and the second is systematic.

4 In Method A, the background contributions from SM γ events and QCD multijet
5 events are expected to reproduce many of the kinematic distributions quite well; for
6 example, photon E_T and various invariant masses. Nonetheless, the PYTHIA Monte
7 Carlo event generator used to generate the MC data samples includes only leading-
8 order Feynman diagrams, and this limitation may be apparent in distributions like H_T
9 that rely on the accurate modeling of subleading jets.

10 **Method B:** In an attempt to overcome the limitations of using a leading-order
11 Monte Carlo generator to model jet properties in $\gamma + \text{jets}$ events, we implement a
12 novel method in which the QCD multijet events from the sideband data are used as a
13 substitute for the PYTHIA SM γ events. Although the QCD multijet events originate
14 from a different physical process than prompt $\gamma + \text{jets}$ events, we hypothesize that

these events, which come from actual data, describe the properties of jets in $\gamma + \text{jets}$ events better than leading-order Monte Carlo. This should be readily apparent in distributions such as H_T and the number of jets in the event.

Since the sideband data presumably do not contain actual prompt photons, and are only QCD background, we do not expect the reconstructed “QCD photons” in those events to have the same E_T distribution as the actual prompt photons from PYTHIA. We therefore weight the events in the QCD background template in such a way that the weighted QCD template matches the sum of the PYTHIA SM γ and QCD templates for the photon E_T distribution. For an event in bin i of the photon E_T distribution, the associated weight is

$$w_i = \frac{N_i^{SM\gamma} + N_i^{QCD}}{N_i^{QCD}} \quad (4)$$

where $N_i^{SM\gamma}$ and N_i^{QCD} are the contents of each bin i of the background templates determined using Method A. Using Eq. 4, a unique weight can be assigned to every event in the QCD background sample based on the bin i of the QCD photon E_T .

By defining a weight in this manner for every QCD background event, the QCD background template can be weighted for every kinematic distribution. In all of the kinematic distributions, the weighted QCD template replaces the standard QCD template and the SM γ template. In the case of photon E_T , by definition, the weighted QCD background template will be identical to the sum of the SM γ and QCD templates.

This weighting procedure is referred to as Method B. The weighted QCD template is normalized so that the total number of events, $N^{\text{Weighted-QCD}}$, satisfies:

$$N^{\text{Data}} = N^{\text{Weighted-QCD}} + \underbrace{N^{\text{Di-}\gamma}}_{\text{fixed}} + \underbrace{N^{\text{EWK}}}_{\text{fixed}} + \underbrace{N^{\text{Non-collision}}}_{\text{fixed}}. \quad (5)$$

As in Method A, we force the total number of background events to be equal to the total number of data events in each data sample studied. We have calculated an additional systematic uncertainty for weighting procedure, and it is included in the plots of Method B distributions.

Table 3 summarizes the Method B background estimates for the $\gamma + \geq 1$ jet and $\gamma + \geq 2$ jet samples. Table 4 summarizes the Method B background estimates for the $\gamma + \geq 1$ jet + $\cancel{E}_T > 20$ GeV and $\gamma + \geq 2$ jet + $\cancel{E}_T > 20$ GeV samples.

5 Systematic Uncertainties

The following systematic uncertainties are studied and a scale for each uncertainty is derived using different techniques. Any correlation across bins is ignored and all errors are added in quadrature to calculate the total systematic uncertainty. We have followed standard practices of quoting systematic uncertainties. All systematic uncertainties quoted are one standard deviation ($\pm 1\sigma$) unless described otherwise.

Background	$\gamma + \geq 1$ Jet Sample	$\gamma + \geq 2$ Jet Sample
QCD (weighted)	$4859511 \pm 2204 \pm 149665$	$903250 \pm 950 \pm 44525$
Electroweak	$11765 \pm 108 \pm 952$	$1833 \pm 42 \pm 271$
Diphoton	$12136 \pm 110 \pm 641$	$1775 \pm 42 \pm 196$
Non-Collision	$132 \pm 11 \pm 4$	$8 \pm 2 \pm 1$
$\gamma + \mathbf{jets\ Data}$	4883544 ± 2209	906866 ± 952

Table 3: Summary of background estimates for the $\gamma + \geq 1$ jet and $\gamma + \geq 2$ jet data samples evaluated by Method B. Where two uncertainties are quoted, the first is statistical and the second is systematic.

Background	$\gamma + \geq 1$ Jet + $\cancel{E}_T > 20$ GeV Sample	$\gamma + \geq 2$ Jet + $\cancel{E}_T > 20$ GeV Sample
QCD (weighted)	$127405 \pm 357 \pm 7040$	$40887 \pm 202 \pm 2103$
Electroweak	$6271 \pm 79 \pm 613$	$843 \pm 29 \pm 122$
Diphoton	$355 \pm 19 \pm 13$	$86 \pm 9 \pm 8$
Non-Collision	$124 \pm 12 \pm 4$	$8 \pm 3 \pm 1$
$\gamma + \mathbf{jets\ Data}$	134155 ± 366	41824 ± 204

Table 4: Summary of background estimates for the $\gamma + \geq 1$ jet + $\cancel{E}_T > 20$ GeV and $\gamma + \geq 2$ jet + $\cancel{E}_T > 20$ GeV data samples evaluated by Method B. Where two uncertainties are quoted, the first is statistical and the second is systematic.

The uncertainty in determining corrections to jet energies is taken into account as it changes the signal acceptance and the trigger efficiency, and hence the measured kinematic distributions. Uncertainties due to jet energy mismeasurements are obtained by varying the corrected jet energy by one standard deviation from the mean corrected value, $+\sigma$ and $-\sigma$. A new set of events are selected from this shifted jet energy data. Each variation is compared to the nominal value, and the maximum deviation from the nominal value is taken as the systematic uncertainty. The jet energy scale is by far the largest uncertainty in most of the measured distributions.

The uncertainty in the determination of the true photon fraction is described in literature [4] and is taken into account as follows. The normalization of the QCD template and the SM prompt photon template is changed by $\pm\sigma = \pm 0.068$ from the nominal value of the fake photon fraction, which is defined in Eq. ???. For each histogram bin, the maximum difference between the nominal distribution and the two varied ($\pm\sigma$) distributions is taken as the systematic uncertainty. This uncertainty makes a moderate contribution to the total systematic uncertainty. This uncertainty increases from about 10% to about 40% with increasing photon E_T .

The uncertainty in the choice of photon sideband to represent the fake jets in the tight photon sample is estimated by varying the loose photon selection requirements to

match the tight photon ID selection requirements. By doing so, one probes the sideband sample for the correlation to the tight photon sample. The selection requirements, Isolation Energy (E_T^{Iso}), Had/Em (E_{HAD}/E_{EM}), Track p_T , and Track Isolation are common to both loose and tight photon selection requirements. Each of these loose photon selection requirements is set equal to the tight photon selection requirements one at a time, and four new sideband samples are selected. New samples are normalized back to the original (nominal) sideband sample and compared. The maximum deviation of each varied sample from the original sample is taken as the systematic uncertainty.

The acceptance and trigger efficiency depends on the Parton Distribution Functions (PDFs). The uncertainty in the PDFs used in MC event generation is derived following the recommendations of the CDF Joint Physics Group. Instead of generating many different sets of Monte Carlo event samples for each PDF set, CTEQ5L events are reweighted to CTEQ6M (next-to-leading order PDFs). The initial parton's information is approximated using generator-level information and 40 (+1) weights are generated for each of the 20 eigenvectors (higher and lower than nominal) and for a base distribution. Each kinematic distribution is remade according to the 40 (+1) generated weights. A maximum of 2 variations for each weight (representing an eigenvector) are added in quadrature to derive the total uncertainty. They are added in quadrature because these 20 eigenvectors are independent.

The dependence on the renormalization, factorization, and fragmentation scales (Q^2) are varied to estimate the higher-order contributions not considered by using leading-order MC signal sample. Two MC samples are generated by varying the nominal scale by 0.5 and 2.0. Each varied sample is normalized back to the nominal sample and the difference in shape from the nominal shape is taken as the systematic uncertainty. This systematic uncertainty is derived using only the generator-level objects. The leading photon is identified using generator-level information and hadron-level jets are used.

Uncertainty in the the amount of radiation from the incoming and outgoing partons is estimated by varying the corresponding PYTHIA parameters following the Joint Physics Group's recommendations. Five MC samples (more ISR, less ISR, more FSR, less FSR, and nominal) were needed. The MC samples for each variation are really a combination of many different MC sample with different \hat{p}_T , which are normalized by cross section to get the complete spectrum. Each of the four variations is normalized to the nominal distribution and the maximum variation of ISR and FSR is added in quadrature to derive the total systematic uncertainty.

The value of the strong coupling constant (α_s) used in the generation of Monte Carlo event samples is not measured directly or absolutely. It is measured at the masses of the π^0 and Z -boson and then extrapolated to the other regions. An uncertainty for this is derived by comparing CTEQ5L PDF-based Monte Carlo events to MRST98 PDF-based Monte Carlo events, which use different values of α_s when generating events.

The uncertainty in the measurement of the luminosity is approximately 6% [9]. Whenever a MC event sample is normalized by the luminosity, the uncertainty in the luminosity measurement needs to be taken into account. This is done by changing

the luminosity by $\pm 6\%$ and recalculating the measurement. For every histogram bin, the maximum difference between these altered measurements and the nominal measurement is taken as the uncertainty due to the luminosity. The contribution of this uncertainty to the total uncertainty is relatively small.

The energy measured by the EM calorimeter carries a 1% uncertainty. Hence, the photon candidate's energy is shifted by $\pm 1\%$ and compared to the nominal distribution. The difference is taken as the systematic uncertainty due to the EM energy measurement.

As for the initial test methods, the statistical uncertainty in the cosmic photon template is taken as the systematic uncertainty for that bin. This uncertainty is very small and becomes somewhat significant in the high- \cancel{E}_T region in the \cancel{E}_T measurement.

Beam halo background is a very small background, and a constant 50% uncertainty is assigned for its estimate.

In addition to above uncertainties, the uncertainty in the reweighting of the sideband events used in Method B is derived by varying the fake photon fraction by its systematic uncertainty. This will change the fraction of SM γ and QCD events chosen. The sideband events are reweighted using these alternate weights and the difference between these and the nominal distribution is taken as the uncertainty. This uncertainty increases from a few percent to about 10% with increasing photon E_T .

The JES is the largest systematic uncertainties in most of the measured distributions.

6 Results

We present results in the $\gamma + \text{jets}$ data with and without the $\cancel{E}_T > 20$ GeV requirement. In the $\gamma + \geq 1$ jet and $\gamma + \geq 2$ jet event samples, we measure the E_T of the photon, the E_T of the leading jet, H_T (scalar sum of all EM objects, jets and \cancel{E}_T), \cancel{E}_T , and invariant mass of photon and leading jet. In addition, in the $\gamma + \geq 2$ jet sample, we measure the invariant mass of the photon + two leading jets and the invariant mass of the two leading jets.

Figures 2–5 show Method A results without the \cancel{E}_T requirement, and Figures 6–9 show Method A results with the \cancel{E}_T requirement. The data are represented by black circles, and the backgrounds are shown in different colors. As described in Section 4, the SM backgrounds include prompt γ production (labeled “ γ MC”), QCD multi-jet production (labeled “QCD”), prompt diphoton production (labeled “Di- γ ”), and electroweak production (labeled “EWK”). The non-collision backgrounds from cosmic rays and the beam halo are labeled “Non-collision.” The top plot uses a logarithmic scale. The shaded region indicates the total systematic uncertainty, which includes the statistical uncertainty on the total background prediction.

The uncertainty due to the jet energy scale is by far the largest systematic uncertainty. Other sources of uncertainty that are taken into account include the following: parton density functions (PDFs), initial and final state radiation (ISR/FSR), depen-

dence on the renormalization, factorization and normalization scales (Q^2), the strong coupling constant (α_s), the fake photon fraction determination, integrated luminosity, EM energy measurements, the beam halo estimate, and the cosmic ray background estimate.

We have measured the photon E_T spectrum from 30 GeV to about 550 GeV, and over this range the total systematic uncertainty increases from 15% to 90%. It is evident that the photon purity increases at higher E_T . We are limited by statistics at high E_T . The invariant mass of the γ + leading jet extends up to 1000 GeV/c². Many background predictions become limited by statistics in the high mass region, and the systematic uncertainty increases from 15% to 90%. It is evident from these plots that the SM γ and QCD multijet backgrounds are dominant. However with the requirement of large \cancel{E}_T in the event, these backgrounds are reduced and real \cancel{E}_T from the electroweak processes (*e.g.* $W \rightarrow \ell\nu$) becomes significant. This \cancel{E}_T requirement significantly improves the sensitivity to events in which a heavy particle is produced that we do not detect.

The backgrounds using Method A are well modeled and describe data reasonably well in most of the distributions. But a close inspection reveals discrepancies in certain distributions like lead jet E_T , H_T , jet multiplicity, and \cancel{E}_T , which are not within the systematic uncertainties. These kinematic distributions are most directly affected by the limitations of the leading-order predictions using PYTHIA.

Figures 10–13 show the Method B results without the \cancel{E}_T requirement. The Figures 14–17 show the Method B results with the \cancel{E}_T requirement. In these figures, “QCD (weighted)” indicates the weighted QCD background template that replaces the γ MC and QCD templates of Method A. Using Method B, we are able describe some distributions much better compared to Method A. The photon E_T distribution must agree with Method A by construction. The jet E_T , H_T , jet multiplicity and \cancel{E}_T distributions, however, show significant improvement and agree well with data. The \cancel{E}_T distribution agrees well in the low \cancel{E}_T region. Some distributions using Method B were not modeled well as expected. For example the invariant mass of the photon and leading jet shows a large discrepancy, which is attributed to the fact that the QCD background events are from different processes (or Feynman diagrams).

7 Conclusions

We have presented results of the search for beyond SM physics in γ + ≥ 1 jet and γ + ≥ 2 jet events with and without a $\cancel{E}_T > 20$ GeV requirement. We have presented two different background prediction methods, Method A and Method B. Each method has proven to describe the γ + jets data with certain limitations. We conclude the two methods together provide a greater understanding of data than either method alone. Thus far, we see good agreement with Standard Model predictions extending over several orders of magnitude. The search for new heavy particles in the high \cancel{E}_T events has shown no significant deviation from data. We conclude that all of our

1 measurements are in agreement with the Standard Model expectation.

2 8 Acknowledgements

3 We thank the Fermilab staff and the technical staffs of the participating institutions for
4 their vital contributions. This work was supported by the U.S. Department of Energy
5 and National Science Foundation; the Italian Istituto Nazionale di Fisica Nucleare; the
6 Ministry of Education, Culture, Sports, Science and Technology of Japan; the Natural
7 Sciences and Engineering Research Council of Canada; the National Science Coun-
8 cil of the Republic of China; the Swiss National Science Foundation; the A.P. Sloan
9 Foundation; the Bundesministerium für Bildung und Forschung, Germany; the World
10 Class University Program, the National Research Foundation of Korea; the Science
11 and Technology Facilities Council and the Royal Society, UK; the Institut National de
12 Physique Nucleaire et Physique des Particules/CNRS; the Russian Foundation for Ba-
13 sic Research; the Ministerio de Ciencia e Innovación, and Programa Consolider-Ingenio
14 2010, Spain; the Slovak R&D Agency; and the Academy of Finland.

15 References

- 16 [1] F. Abe *et al.*, Nucl. Instrum. Methods Phys. Res. A **271**, 387 (1988); D. Amidei *et*
17 *al.*, Nucl. Instrum. Methods Phys. Res. A **350**, 73 (1994); F. Abe *et al.*, Phys. Rev.
18 D **52**, 4784 (1995); P. Azzi *et al.*, Nucl. Instrum. Methods Phys. Res. A **360**, 137
19 (1995); The CDF II Detector Technical Design Report, Fermilab-Pub-96/390-E.
- 20 [2] See for example S. Ambrosanio *et al.*, Phys. Rev. D **54**, 5395 (1996); or C.-H.
21 Chen and J.F. Gunion, Phys. Rev. D **58**, 075005 (1998).
- 22 [3] S. Weinberg, “Implications of Dynamical Symmetry Breaking: An Addendum”
23 Phys. Rev. D **19**, 1277–1280 (1979); L. Susskind, “Dynamics of Spontaneous
24 Symmetry Breaking in the Weinberg-Salam Theory” Phys. Rev. D **20**, 2619–2625
25 (1979).
- 26 [4] F. Abe *et al.*, “Prompt photon cross section measurement in $\bar{p}p$ collisions at \sqrt{s}
27 $= 1.8$ TeV”, Phys. Rev. D **48**, 2998–3025 (1993); F. Abe *et al.*, “Precision Mea-
28 surement of the Prompt Photon Cross Section in $p\bar{p}$ Collisions at $\sqrt{s} = 1.8$ TeV”,
29 Phys. Rev. Lett. **73**, 2662 (1994); D. Acosta *et al.* (CDF Collaboration), Phys.
30 Rev. Lett. **95**, 092004 (2007); The CDF Collaboration, “Search for Anomalous
31 Production of Events with a Photon, Jet, b -quark Jet, and Missing Transverse
32 Energy ”, Phys. Rev. D **80** (2009).
- 33 [5] “The Timing System for the CDF Electromagnetic Calorimeters,” Nucl. Instrum.
34 Meth. **A565**, 543–550, 2006.

- 1 [6] M. Goncharov *et al.*, “Discrimination of Beam Halo and Cosmic Rays as a Source
2 of Photon Candidates,” CDF-Note 8409.
- 3 [7] The CDF Collaboration, “Determination of the Jet Energy Scale at the Collider
4 Detector at Fermilab,” Nucl. Instrum. Meth. **A566**, 375–412, 2006.
- 5 [8] T. Sjöstrand *et al.*, Comput. Phys. Commun. **135**, 238 (2001).
- 6 [9] D. Acosta *et al.*, Nucl. Instrum. Methods, **A494**, 57 (2002).
- 7 [10] L. Balka *et al.* Nucl. Instrum. Methods **267**, 272 (1988); S. Bertolucci *et al.* Nucl.
8 Instrum. Methods **267**, 301 (1988); S. Kuhlmann *et al.*, Nucl. Instrum. Methods
9 **518**, 39, 2004.

Figure 2: Kinematic distributions of $\gamma + \geq 1$ jet events using Method A. See Section 6 for a description of the elements in these distributions.

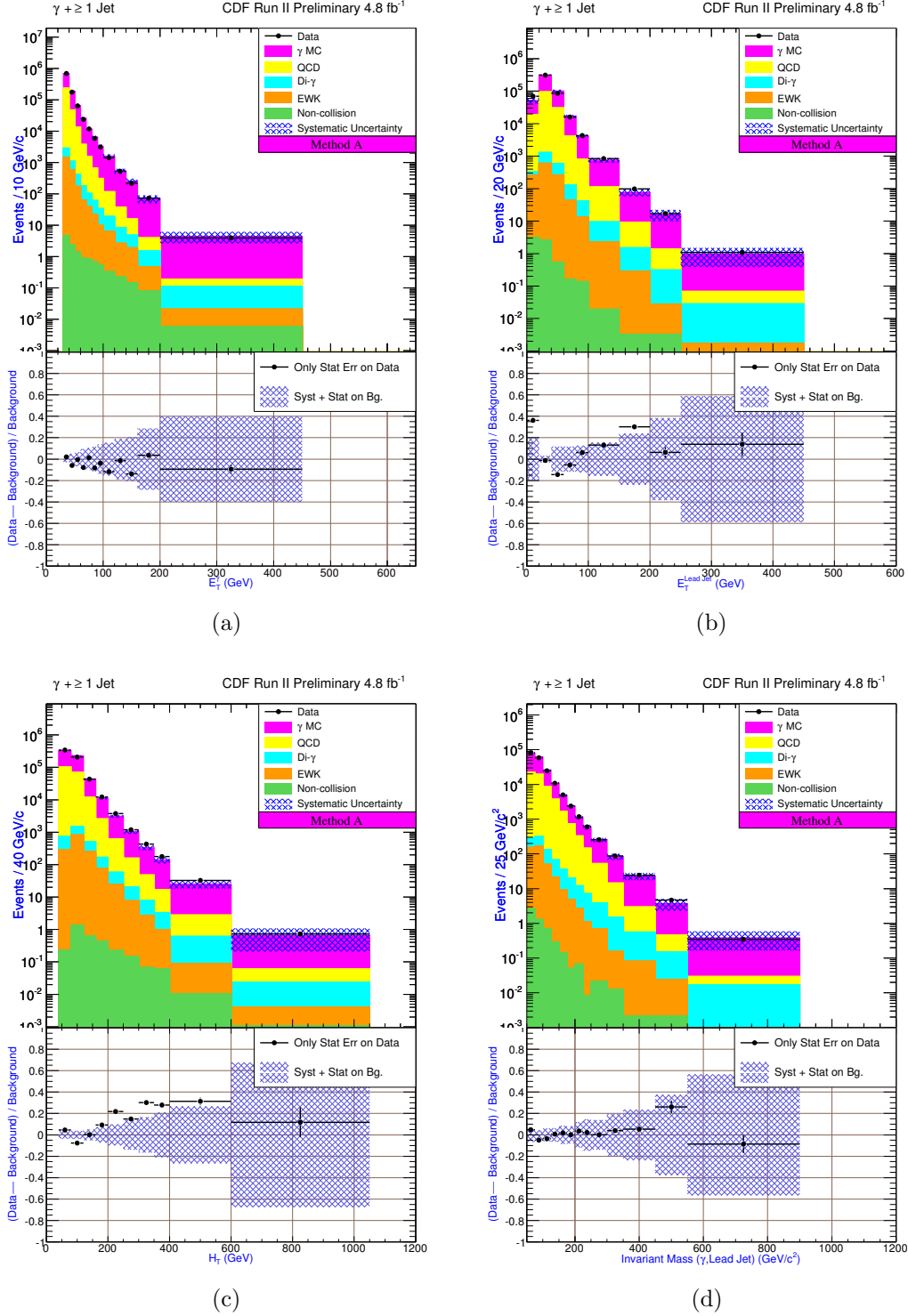


Figure 3: Kinematic distributions of $\gamma + \geq 1$ jet (top) and $\gamma + \geq 2$ jet (bottom) events using Method A. See Section 6 for a description of the elements in these distributions.

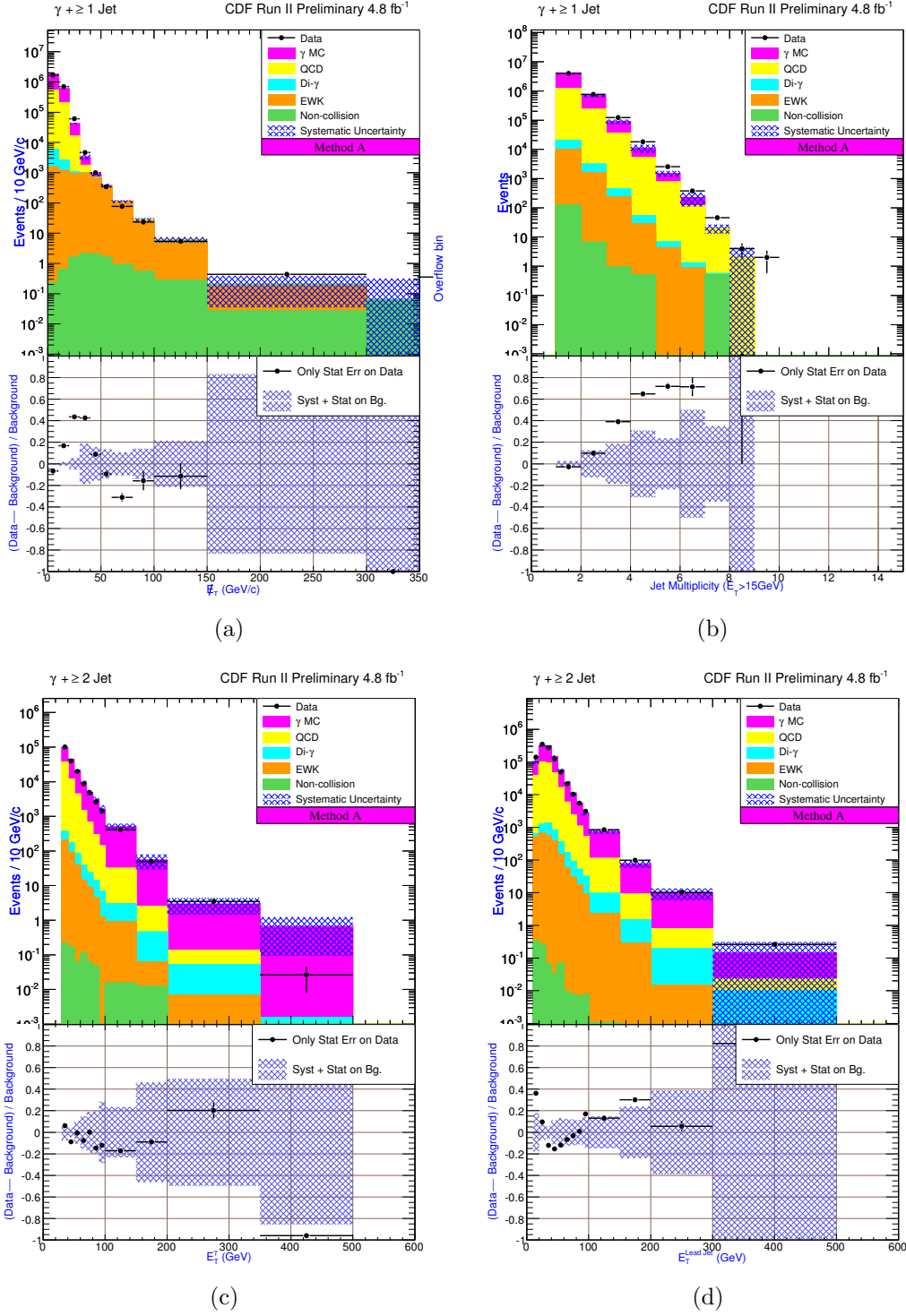


Figure 4: Kinematic distributions of $\gamma + \geq 2$ jet events using Method A. See Section 6 for a description of the elements in these distributions.

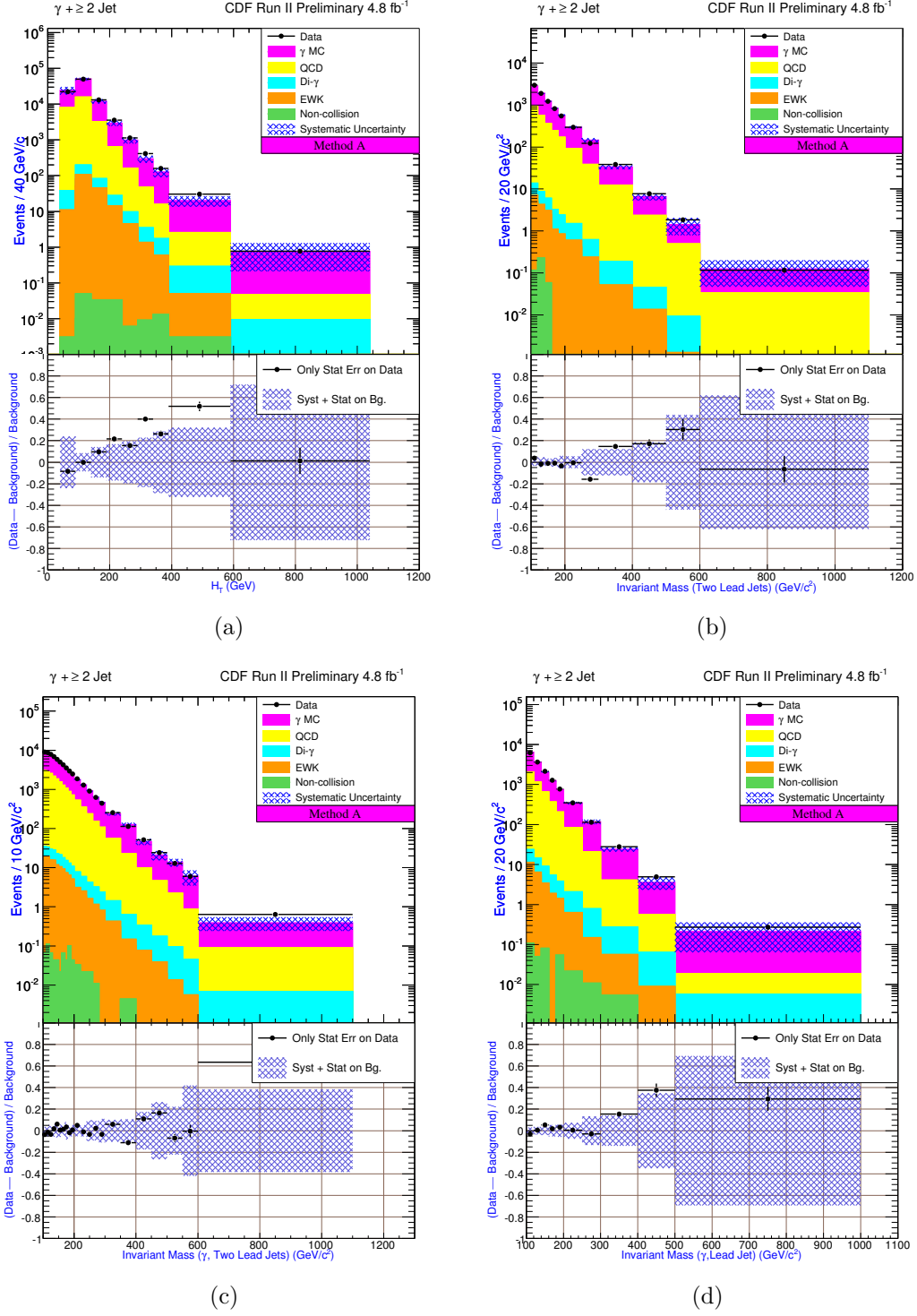
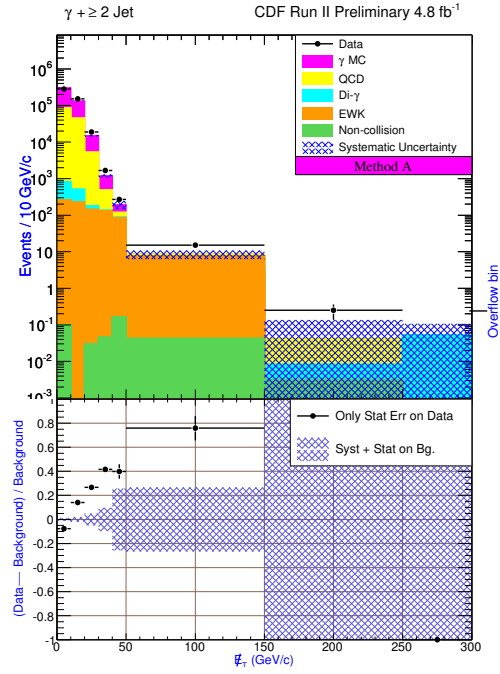


Figure 5: Kinematic distributions of $\gamma + \geq 2$ jet events using Method A.



(a)

Figure 6: Kinematic distributions of $\gamma + \geq 1$ jet + $\cancel{E}_T > 20$ GeV events using Method A. See Section 6 for a description of the elements in these distributions.

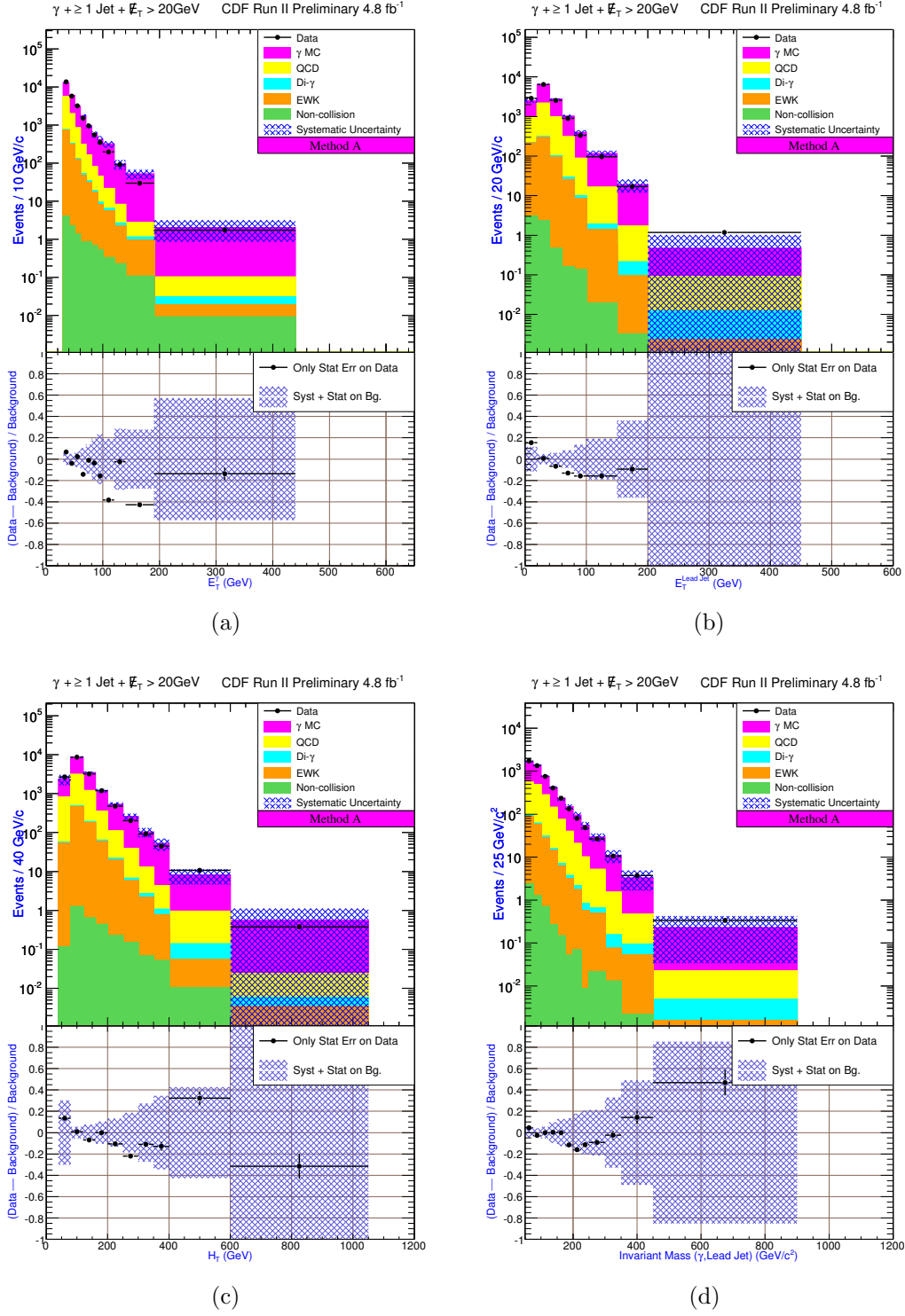


Figure 7: Kinematic distributions of $\gamma + \geq 1$ jet + $\cancel{E}_T > 20$ GeV (top) and $\gamma + \geq 2$ jet + $\cancel{E}_T > 20$ GeV (bottom) events using Method A. See Section 6 for a description of the elements in these distributions.

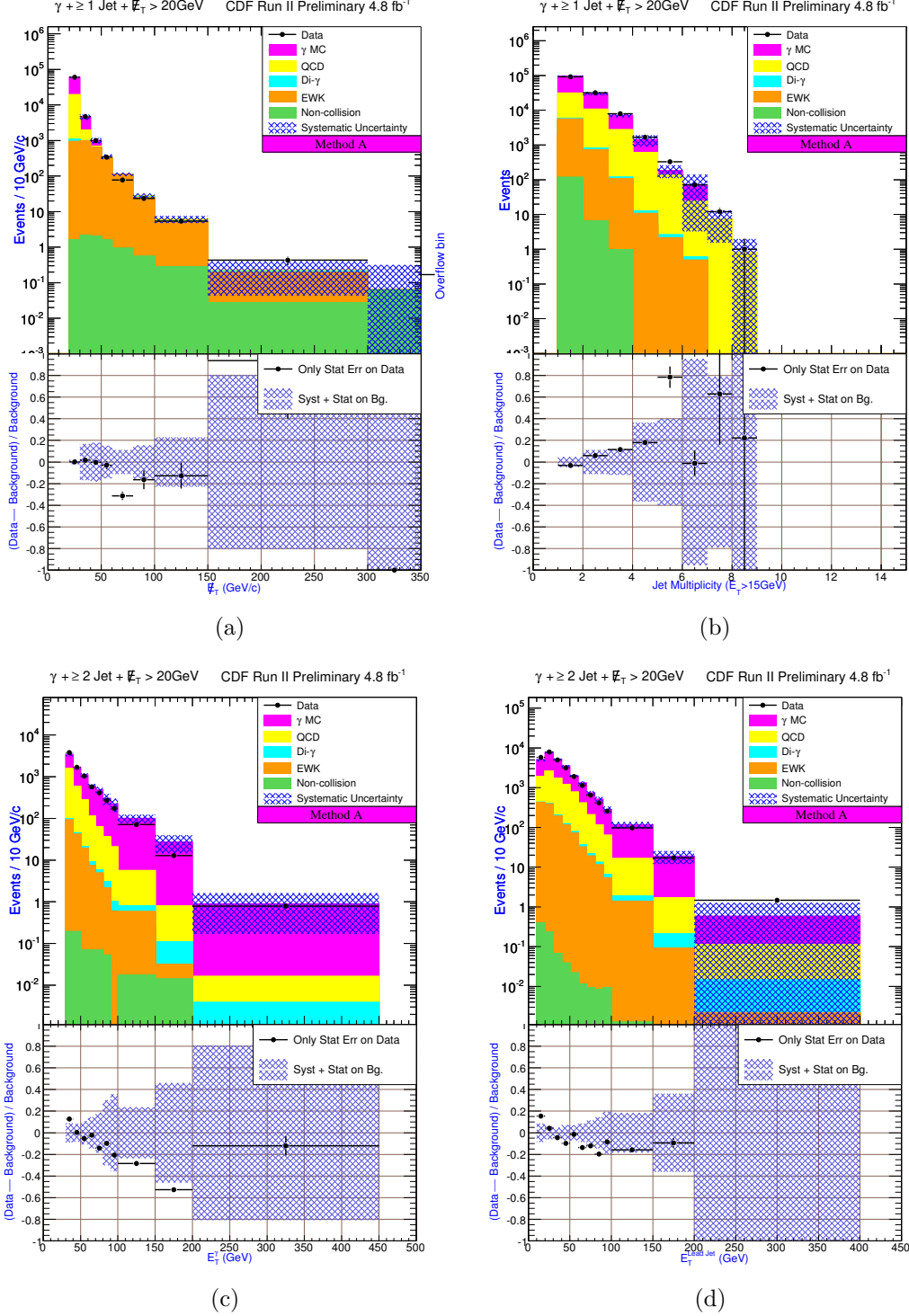


Figure 8: Kinematic distributions of $\gamma + \geq 2 \text{ jet} + \cancel{E}_T > 20 \text{ GeV}$ events using Method A. See Section 6 for a description of the elements in these distributions.

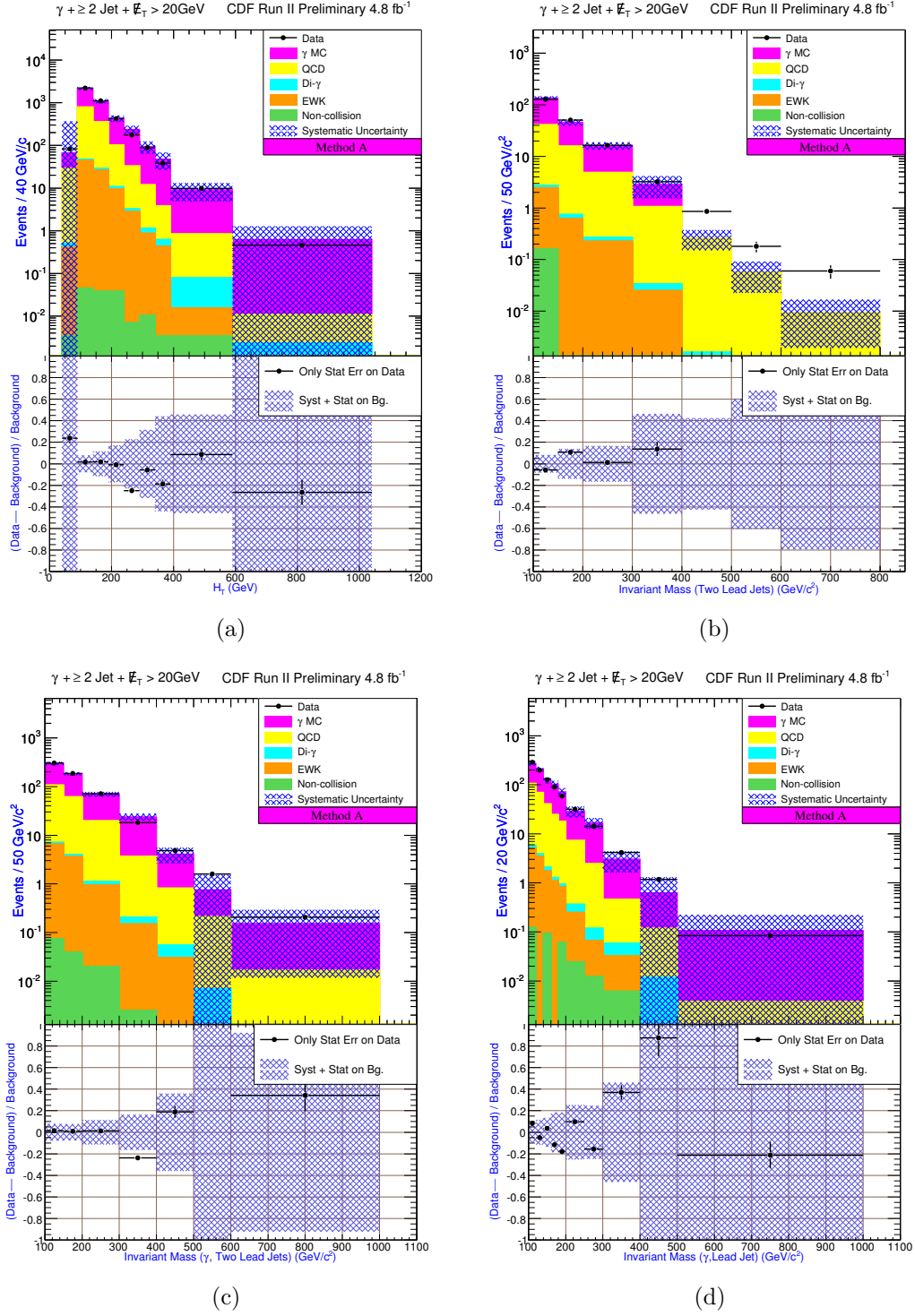


Figure 9: Kinematic distributions of $\gamma + \geq 2 \text{ jet} + \cancel{E}_T > 20 \text{ GeV}$ events using Method A. See Section 6 for a description of the elements in these distributions.

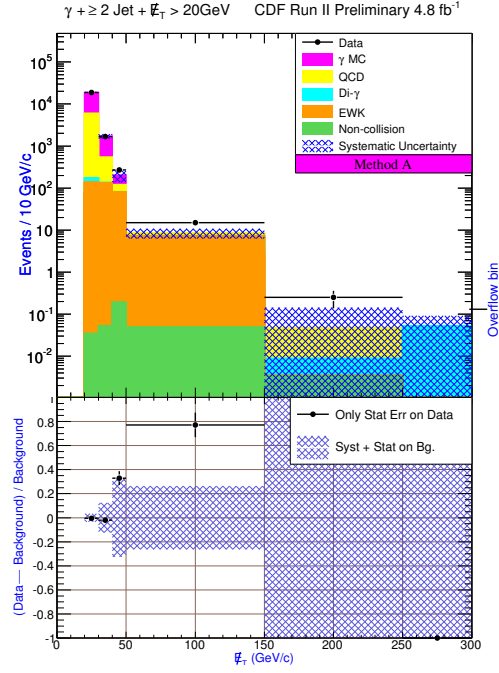


Figure 10: Kinematic distributions of $\gamma + \geq 1$ jet events using Method B. See Section 6 for a description of the elements in these distributions.

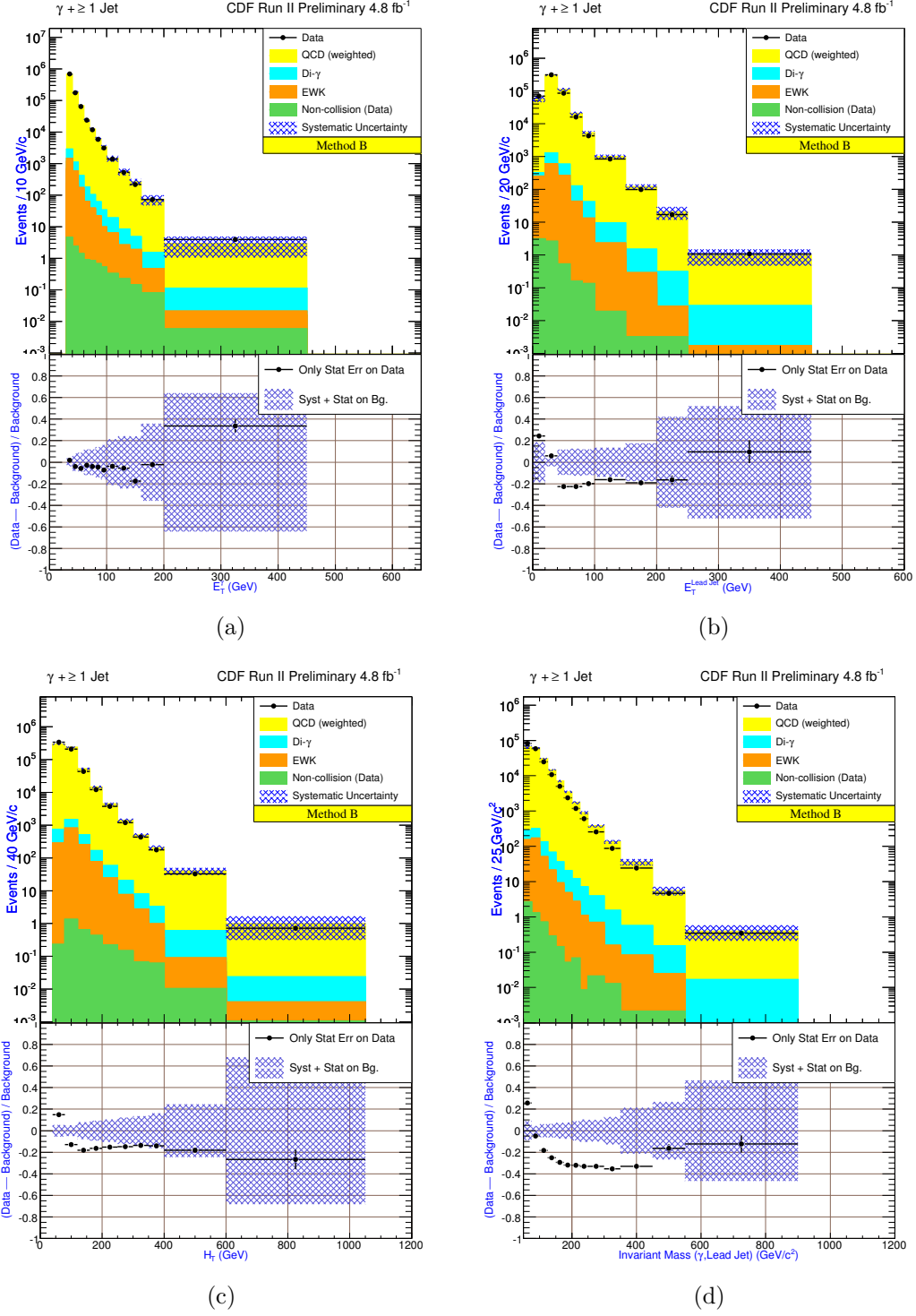


Figure 11: Kinematic distributions of $\gamma + \geq 1$ jet and $\gamma + \geq 2$ jet events using Method B. See Section 6 for a description of the elements in these distributions.

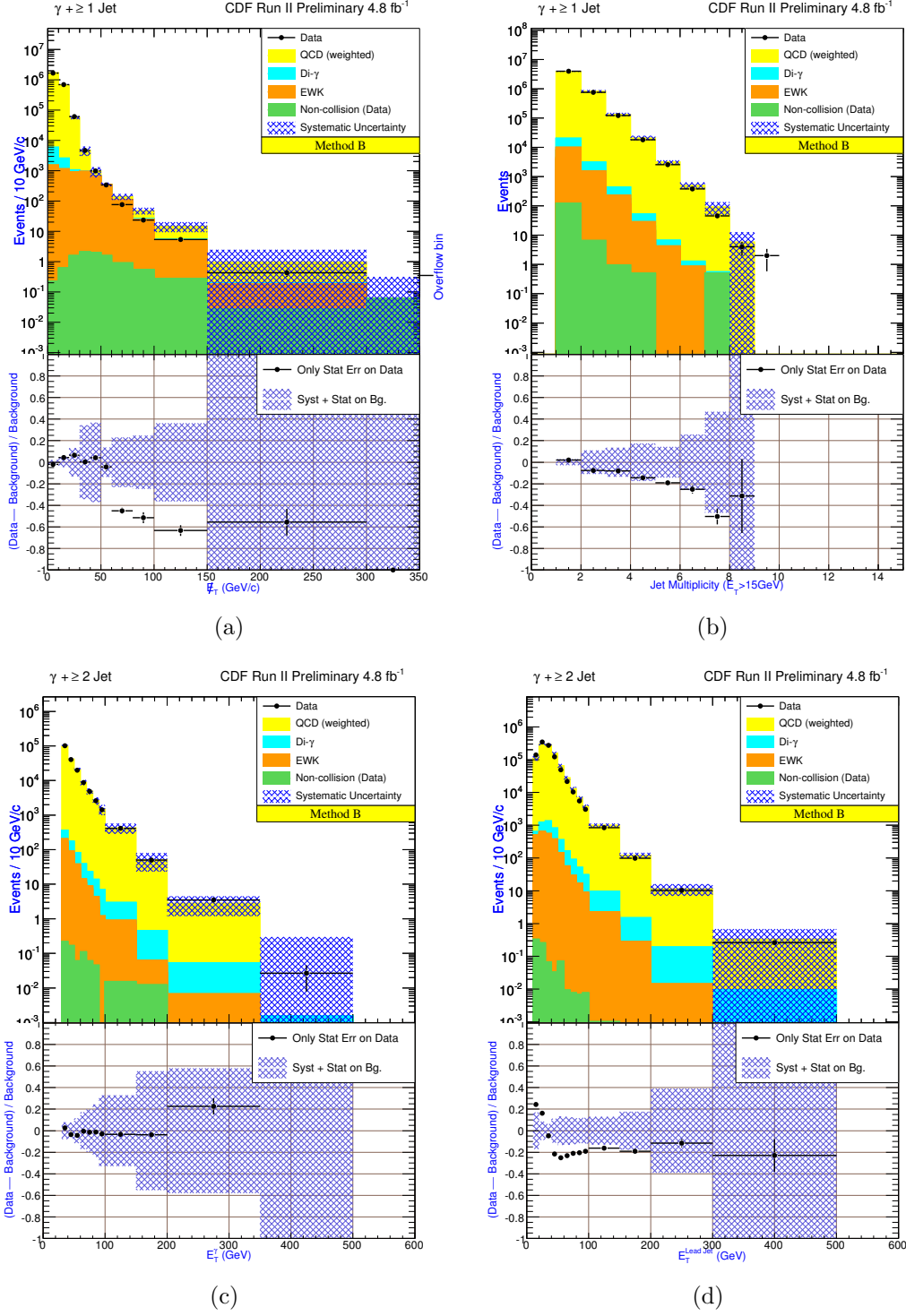


Figure 12: Kinematic distributions of $\gamma + \geq 2$ jet events using Method B. See Section 6 for a description of the elements in these distributions.

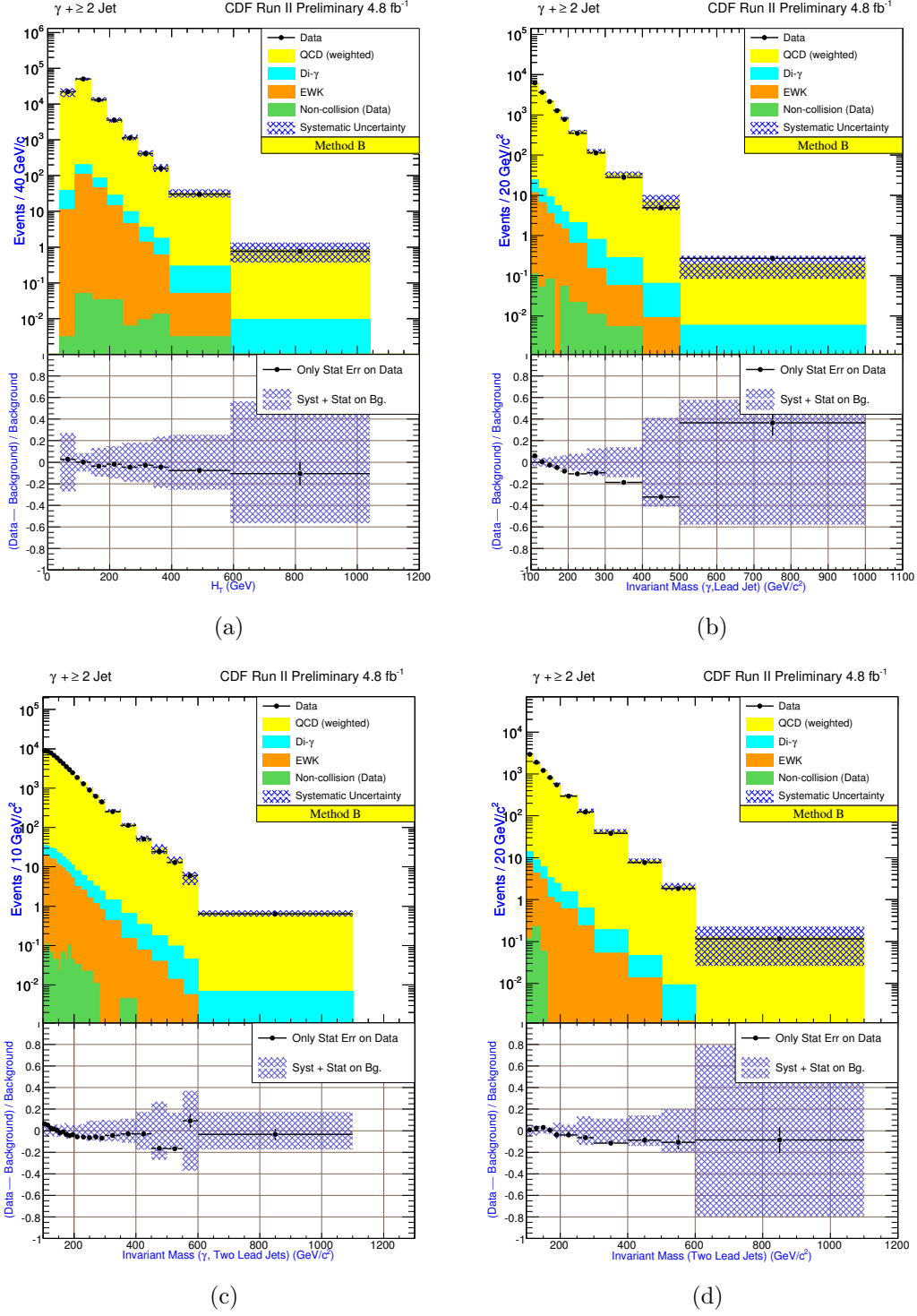


Figure 13: Kinematic distributions of $\gamma + \geq 2$ jet events using Method B. See Section 6 for a description of the elements in these distributions.

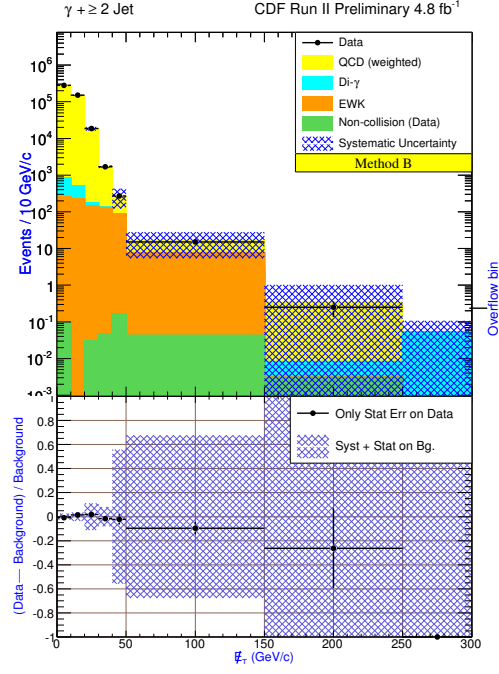


Figure 14: Kinematic distributions of $\gamma + \geq 1$ jet + $\cancel{E}_T > 20$ GeV events using Method B. See Section 6 for a description of the elements in these distributions.

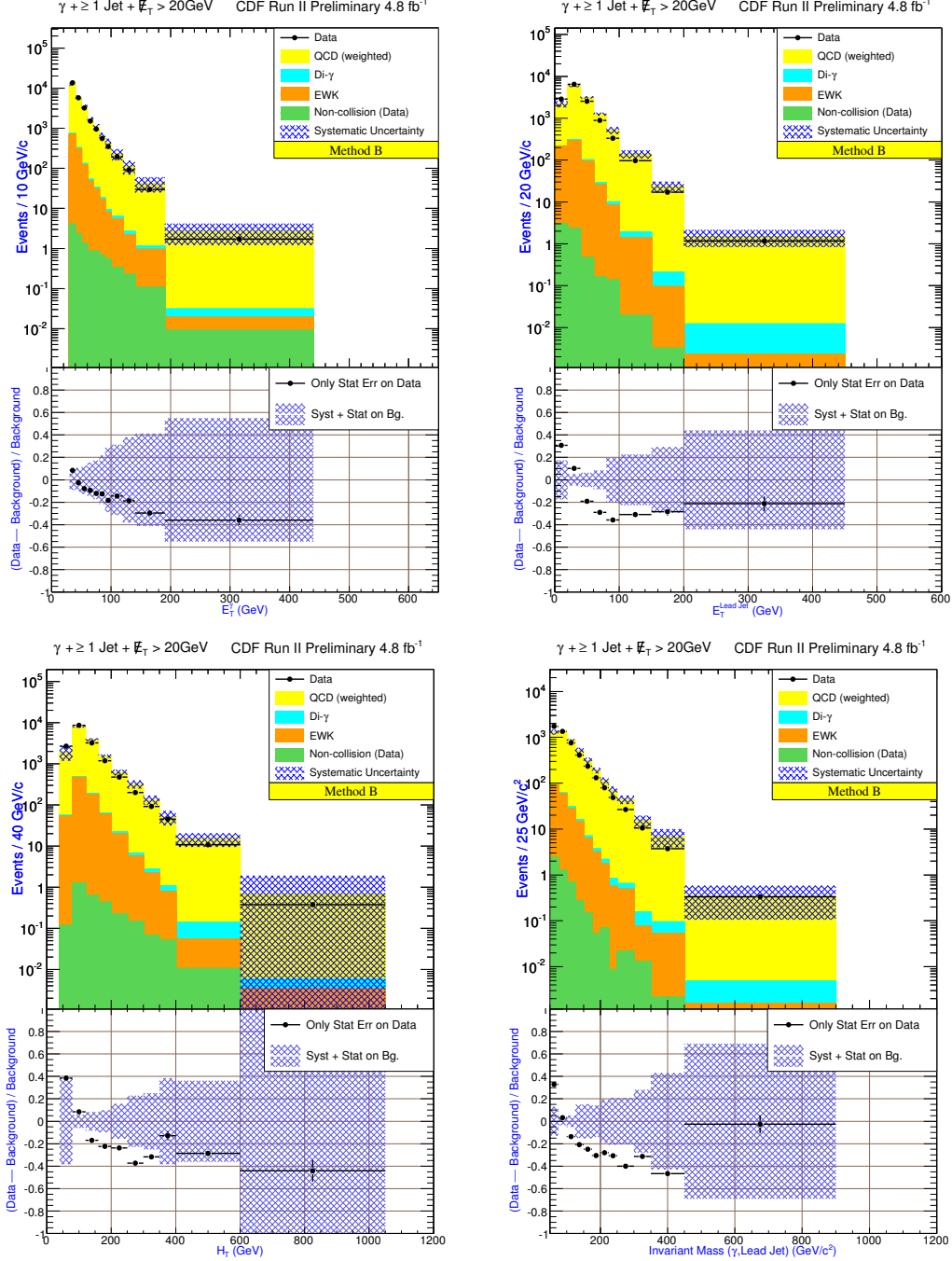


Figure 15: Kinematic distributions of $\gamma + \geq 1$ jet + $\cancel{E}_T > 20$ GeV and $\gamma + \geq 2$ jet + $\cancel{E}_T > 20$ GeV events using Method B. See Section 6 for a description of the elements in these distributions.

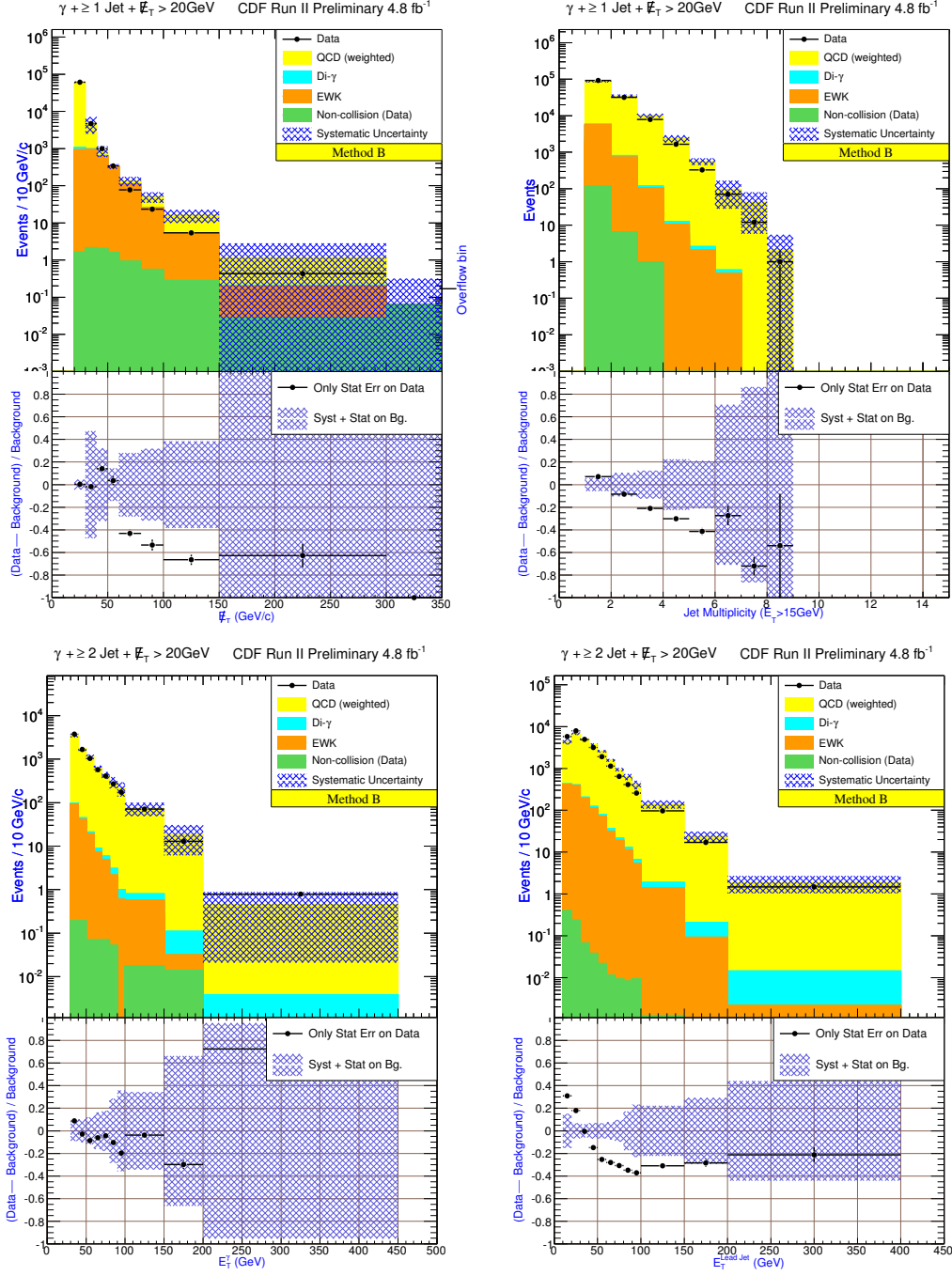


Figure 16: Kinematic distributions of $\gamma + \geq 2 \text{ jet} + \cancel{E}_T > 20 \text{ GeV}$ events using Method B. See Section 6 for a description of the elements in these distributions.

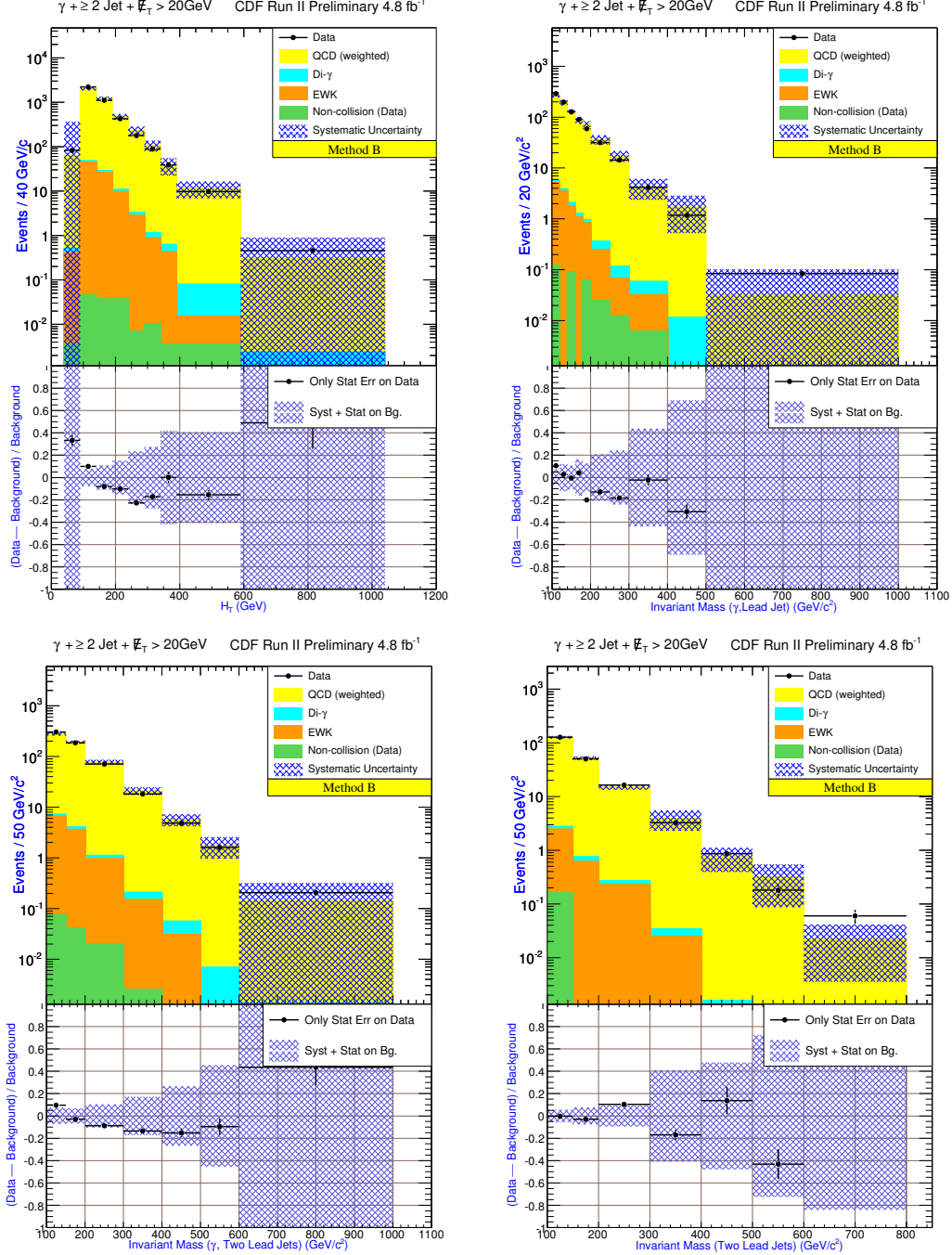


Figure 17: Kinematic distributions of $\gamma + \geq 2 \text{ jet} + \cancel{E}_T > 20 \text{ GeV}$ events using Method B. See Section 6 for a description of the elements in these distributions.

